MATERIALS SCIENCE

Biodegradable origami enables closed-loop sustainable robotic systems

Pingdong Wei[1]†, Zhuang Zhang[2,3]†, Shaoru Cheng[1]†, Yao Meng[1], Mengjie Tong[4], Luoqian Emu[1], Wei Yan[1], Yanlin Zhang[1], Yunjie Wang[1], Jingyang Zhao[1], Changyu Xu[1,3], Feng Zhai[4], Junqiang Lu[5]*, Lei Wang[1,3,6]*, Hanqing Jiang[1,3,7]*

Robots are increasingly integral across various sectors due to their efficiency and superior capabilities, which enable performance beyond human potential. However, the development of robotic systems often conflicts with the sustainable development goals set by the United Nations, as they generate considerable nondegradable waste and organic/inorganic pollutants throughout their life cycle. In this paper, we introduce a dual closed-loop robotic system that integrates biodegradable, sustainable materials such as plasticized cellulose films and NaCl-infused ionic conductive gelatin organogels. These materials undergo a closed-loop ecological cycle from processing to biodegradation, contributing to new growth, while the self-sensing, origami-based robot supports a seamless human-in-the-loop teleoperation system. This innovative approach represents a paradigm shift in the application of soft robotic systems, offering a path toward a more sustainable future by aligning advanced robotic functionalities with environmental stewardship.

INTRODUCTION

Robots, designed as automated machines, are crafted to emulate the functions of humans or other living beings, achieving intelligent actions such as actuation, perception, and collaboration, which are now even more appealing as carriers of embodied intelligence (*1*–*3*). Typically, robots are categorized into rigid and soft robots based on the materials used in their construction (*4*). Rigid-bodied robots, characterized by their stiff metal links and joints, deliver exceptionally precise and efficient performance for specific tasks, making them widely used in advanced manufacturing industries (*5*). Soft robots have thrived in recent decades due to their highly flexible and compliant nature, which are essential for human-friendly human-machine interactions, and left a broader space for innovations on soft materials (*6*–*9*). Presently, synthetic rubbery materials remain the primary components in soft robot production due to their outstanding moldability, elasticity, stability, and multifunctionality (*10*, *11*). Unfortunately, this often leads to sustainability issues, whether in production processes involving toxic compounds (e.g., toluene, hexane, and chloroform) or the final nondegradable products (e.g., polydimethylsiloxane and liquid crystalline elastomers) (*12*–*17*). Although some efforts have been made to develop recyclable or biodegradable gels for soft robots, these typically realized only a single actuating or sensing function. Often, this comes at the expense of the robots' performance due to the weak mechanical properties and structural instability of gels (*18*–*21*). Thus, there is an increasing need to explore mechanically more stable and sustainable materials as well as innovative design methodologies of robust structure to acquire reliable, sustainable, and biodegradable soft robotic system with complete robotic functionalities (*22*).

The significance of innovative structural design in soft robotics using sustainable materials stems from the inherent challenge of achieving the desired 3D configurations with the most sustainable materials, which often lack the necessary plasticity and rigidity. Beyond the direct use of soft materials (e.g., rubbery materials) for soft robots, folding-based methodology, i.e., origami-based technology that transfers two-dimensional (2D) rigid sheets into elaborated 3D structures has attracted considerable attentions. This approach could herald a new era in engineering soft robots using 2D films instead of traditional rubbery materials, thereby bridging the gap between sustainability and soft robotics (*23*, *24*). Cellulose, as one of the world's most abundant renewable resources, stands out as an exceptional material for sustainable technologies due to its low cost, mechanical stability, and biodegradability (*25*–*28*). In addition, both "top-down" dissolving and "bottom-up" self-assembly processes of cellulose-based materials can be carried out in aqueous systems, without using any toxic organic solvents (*29*). Among different forms of cellulose materials, the entirely biodegradable film receives long-lasting attention because of its superior mechanical properties and structural robustness as well as its ability in industrial-scale manufacturing (*30*, *31*). However, cellulose films suffer intrinsic brittleness, which significantly limits the utilization of mechanically strong cellulose films in origami assembly.

In this work, we introduce a strategy for constructing sustainable, entirely biodegradable, and self-sensing origami robots with full robotic functionalities. This is achieved through the development of mechanically robust cellulose films and highly adhesive ionic conductive gelatin organogels (Fig. 1, A to C). This strategy results in a fully sustainable closed-loop soft robotic system that includes two subcycles: First, mechanically strong cellulose films serve as the structural basis of the self-sensing origami module, and second, highly elastic, adhesive, fully biodegradable, ionically conductive gelatin-based gels are applied as a sustainable sensing layer on the cellulose films. These materials can be completely degraded in many mediums, such as sewage, soil, and enzyme (*19*). The feedstocks used in this work are derived from renewable resources, with the cellulose from cotton and gelatin

[1]School of Engineering, Westlake University, Hangzhou, Zhejiang 310030, China. [2]Academy for Engineering and Technology, Fudan University, Shanghai 200433, China. [3]Institute of Advanced Technology, Westlake Institute for Advanced Study, Hangzhou, Zhejiang 310024, China. [4]College of Physics and Electronic Information Engineering, Zhejiang Normal University, Jinhua, Zhejiang 321000, China. [5]School of Mathematics Information, Shaoxing University, Shaoxing, Zhejiang 312000, China. [6]Zhejiang Key Laboratory of Low-Carbon Intelligent Synthetic Biology, Westlake University, Hangzhou, Zhejiang 310030, China. [7]Research Center for Industries of the Future and School of Engineering, Westlake University, Hangzhou, Zhejiang 310030, China.
*Corresponding author. Email: jlu@usx.edu.cn (J.L.); wang_lei@westlake.edu.cn (L.W.); hanqing.jiang@westlake.edu.cn (H.J.)
†These authors contributed equally to this work.

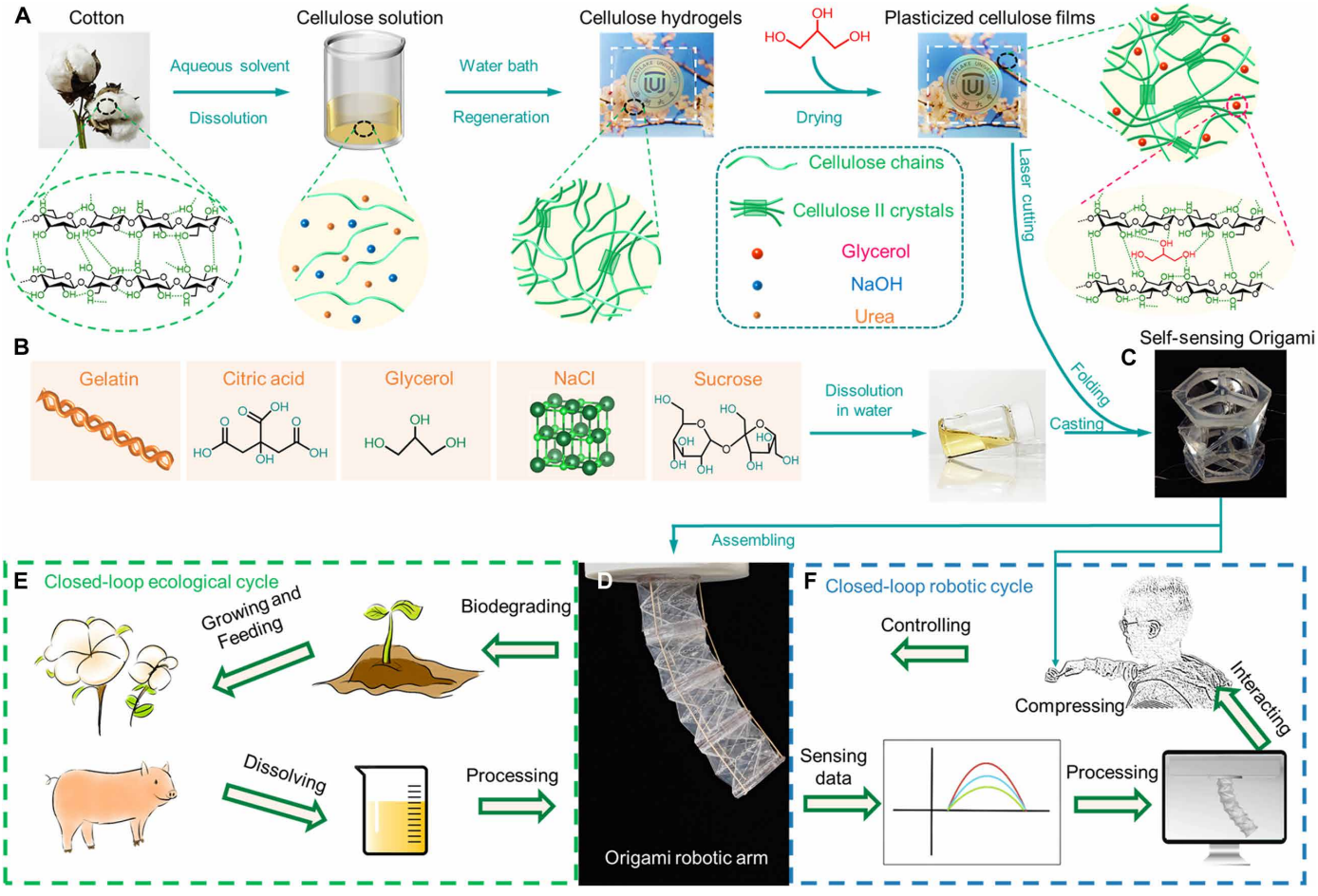

Fig. 1. Conceptual framework of the double-closed-loop robotic systems constructed using sustainable materials. (**A**) Preparation schematic illustration of plasticized cellulose films. (**B**) Ionically conductive gelatin solution. (**C**) Fabricated sustainable self-sensing origami module. (**D**) Modular origami robotic arm. Scheme of the (**E**) closed-loop ecological cycle and (**F**) closed-loop human-robot cycle of the sustainable self-sensing origami systems.

from pork. After usage, these sustainable cellulose films and gelatin gel sensors break down into components that enrich the soil, supporting the growth of new plants and animals, completing a close-loop ecologically cycle (Fig. 1, D to E) (*20*, *32*–*34*). Furthermore, the self-sensing origami modules are versatile, functioning as both a robotic arm and a human-machine interface. This dual functionality facilitates a second cycle within our closed-loop soft robotic system, encompassing actuation, sensation, and interaction, all through the same sustainable material-derived origami modules. The origami modules serve as interfaces not only between humans and robots but also between robots and computers (Fig. 1, D and F). The simplicity and reliability of these closed-loop origami soft robotic systems hold promise for broader applications such as human-machine interactions and robotic teleoperation. Moreover, the use of environmentally friendly materials minimizes the generation of waste, advancing a more sustainable approach to robotic construction and contributing to a sustainable future.

RESULTS

Sustainable and mechanically strong cellulose films

In this study, we propose a sustainable material-based origami module made from cellulose and gelatin as alternatives to unsustainable and nonbiodegradable plastics and sensing materials typically used in soft robotic systems (*6*, *12*, *35*, *36*). To create this module, cellulose is dissolved in an aqueous NaOH/urea solvent system to form a transparent, homogeneous cellulose solution. The solution is then cast and immersed in deionized water for regeneration. During this process, cellulose chains self-assemble into cellulose nanofibers and cellulose II crystallite hydrates. The physical crosslinking (such as hydrogen bonding interactions) and chain entanglements form during the regeneration process result in semitransparent cellulose hydrogels (fig. S1). The intrinsic semi-rigidity and abundant hydrogen bonding sites of the cellulose chains yield strong cellulose films. However, they lack crack-extension tolerance; therefore, the cellulose hydrogels are solvent-exchanged with an aqueous glycerol solution. Adding glycerol as a plasticizer diminishes the strong hydrogen bonding interactions between the semi-rigid cellulose chains, resulting in transparent, plasticized cellulose films after oven drying (Fig. 1A and fig. S1).

The soil degradation test is carried out to evaluate the biodegradation ability of our plasticized cellulose films compared with paper and polyethylene terephthalate (PET), which are commonly used in constructing origami structures. Details of the environment and temperature during the experiment are provided in fig. S2. As the degradation time progresses, both the plasticized cellulose films and paper sheets gradually shatter and degrade, whereas the structural

integrity of PET remains intact (Fig. 2A). Scanning electron microscopy (SEM) is applied to visualize the microstructure change during the degradation test. Initially, both PET and cellulose sheets display smooth and flat surfaces, while paper sheets show large microfibers (Fig. 2B, left). Over time, micro-holes and fibrous structure begin to form on the surface of both the paper and plasticized cellulose films, eventually leading to the collapse of their inner structures (Fig. 2B, middle and right). In contrast, PET remains its structure integrity with a consistently flat and smooth surface throughout the biodegradation process. The biodegradation test confirms the excellent biodegradability of our plasticized cellulose films, attributed to the enriched microorganisms in the soil, whereas PET shows no degradation at all during the test. The weight loss curves, plotted as a function of degradation time, further confirm the film's excellent biodegradability; the plasticized cellulose film loses 21.4% of its weight in the first week, escalating to 98.8% by week 8 (Fig. 2C). For comparison, paper loses 12.3% in the first week and 88.2% by the eighth week. Conversely, PET shows no weight loss over the 8 weeks.

Life cycle assessment (LCA) boundary and results of cellulose film are shown in the Fig. 2 (D and E) and fig. S3, where the positive values are environmental burdens, while the negative values represent credits from biogenic carbon sequestration. The major contributors to the global warming potential (GWP) of plasticized cellulose film are cotton pulp, chemical consumption (NaOH and urea), followed by electricity and heat. These are also major contributors to *Eucalyptus* and softwood cellulose films (Fig. 2D) (*37*, *38*). The GWP of plasticized cellulose films is lower than those of *Eucalyptus* and softwood cellulose films due to lower electricity consumption. We also conduct scenarios to vary energy sources to renewables (including solar electricity and biomass heat), and the GWP can be reduced from 5.69 to 5.09 kg CO_2/kg. For other LCA indicators, cotton cellulose films outperform *Eucalyptus* and softwood cellulose films in abiotic depletion fossil fuels (ADP, fossil fuels), global warming potential (GWP), acidification (AP), photochemical oxidation (POCP), and human toxicity (HTP) but less competitive in abiotic depletion (ADP elements), eutrophication (EP), fresh water aquatic ecotoxicity (FETP), and terrestrial ecotoxicity (TEPT) due to high consumption of fertilizers and herbicides during the cotton cultivation. Compared to conventional plastic films, plasticized cellulose films outperform poly(butylene adipate-*co*-terephthalate) (PBAT) in GWP, ozone layer depletion (ODP), and HDP due to the plastic pellets and higher energy consumption in PBAT production (Fig. 2E and tables S3 and S4) (*39*). However, the other environmental impact indicators of plasticized cellulose film are less competitive with those of PLA, PET, and PVC films due to lower chemical and electricity consumption in their scalable production processes. Overall, the physical properties of cellulose films are comparable to those of traditional films, and they have advantages in terms of biodegradability, biocompatibility, and sustainability. The gaps between cellulose and traditional plastic films can be overcome by further improvements in the cellulose film manufacturing process and the adoption of renewable energy sources.

The abundant hydrogen bonding interactions between glycerol and cellulose chains are confirmed using attenuated total reflectance Fourier-transform infrared spectroscopy (ATR-FTIR; Fig. 2D). The intensity of the characteristic peak at around 3328 cm^{-1} (corresponding to the O-H stretching of hydroxyl groups) notably increases and shifts to a lower wave number of 3306 cm^{-1} after the introduction of glycerol into the cellulose films. This shift confirms the formation of strong hydrogen bonding interactions between glycerol molecules and cellulose chains (*40*). In addition, the wide-angle x-ray diffraction (WAXD) profiles of the pristine cellulose films exhibit three peaks at 12.0°, 20.1°, and 21.4°, corresponding to the reflections from the $(1\bar{1}0)$, (020), and (110) planes in cellulose II crystals, respectively (Fig. 2E). After plasticization, the intensities of these peaks in the plasticized cellulose films substantially weaken; the crystallinity index decreases from 57 to 46%. This reduction can be attributed to the pronounced competing hydrogen bonding interactions between cellulose chains and glycerol molecules, which adversely affect the formation of the inter- and intramolecular hydrogen bonds essential for the recrystallization of cellulose chains (*41*).

Sustainable and reliable origami structure

To create an origami structure, the mechanical properties (e.g., toughness) of the base materials are crucial. Initially, a tearing test is conducted to evaluate the toughness of the cellulose films (Fig. 2F). Pristine cellulose films show a fracture energy of 1.57 kJ/m^2, attributable to the strong physical interactions (e.g., hydrogen bonding interactions and chain entanglements) among the semi-rigid cellulose chains. In contrast, plasticized cellulose films exhibit a remarkably higher fraction energy of 2.67 kJ/m^2, which is 70% higher than that of the pristine films. This considerable increase in fracture energy is due to the softening effects of the glycerol-cellulose chain hydrogen bonding interactions. Moreover, the substantial toughening effect is further evaluated by imaging the fracture cross section morphology of the cellulose films following the tearing tests (Fig. 2, G to I). Pristine cellulose films present a densely packed, coarse morphology characteristics of relatively brittle materials (Fig. 2G). However, plasticized cellulose films reveal a distinct coarse lamellar fracture morphology with many fibril bundles pulled out from the fracture surface (Fig. 2, H to I), contributing to the substantial toughening effect of the cellulose films.

A reliable origami structure requires a robust polymer film capable of withstanding cyclic folding and unfolding. The tensile mechanical properties of the cellulose films reveal that pristine cellulose films exhibit a high tensile strength and Young's modulus, measuring 86 ± 5 MPa and 3.5 ± 0.2 GPa, respectively (Fig. 3A and fig. S4A). However, the remarkable plasticizing effect of glycerol on cellulose films results in a notable reduction in both tensile stress and Young's modulus to 48 ± 3 MPa and 0.9 ± 0.1 GPa, respectively. Furthermore, the elongation at break substantially increases from 21 ± 2% to 43 ± 4% (fig. S4B), indicating a substantial improvement in the flexibility of plasticized cellulose films. The tensile strength of the cellulose films were among the highest value to commonly used biodegradable materials, such as sodium alginate films, sodium carboxymethyl cellulose (CMCNa) films made in the laboratory, and commercially available polylactic acid (PLA) films and Ecovio films (*42*), PBAT films (*43*), while the elongation at break were quite low (fig. S5). In addition, the work of fracture slightly increases from 13.6 ± 0.2 MJ/m^3 in pristine films to 14.5 ± 0.3 MJ/m^3 in plasticized films (fig. S4B), confirming the formation of abundant hydrogen bonding interactions between cellulose chains and glycerol molecules (*44*). The high flexibility of plasticized cellulose films allows for testing of cyclic performance under stretching (Fig. 3B). Large hysteresis loops observed between each loading-unloading cycle further demonstrate the plasticity of the plasticized films, attributable to the dynamic breaking-reforming process of the pronounced hydrogen bonding interactions within the physically crosslinked cellulose network (*45*). Moreover, the mechanical properties of the plasticized cellulose films

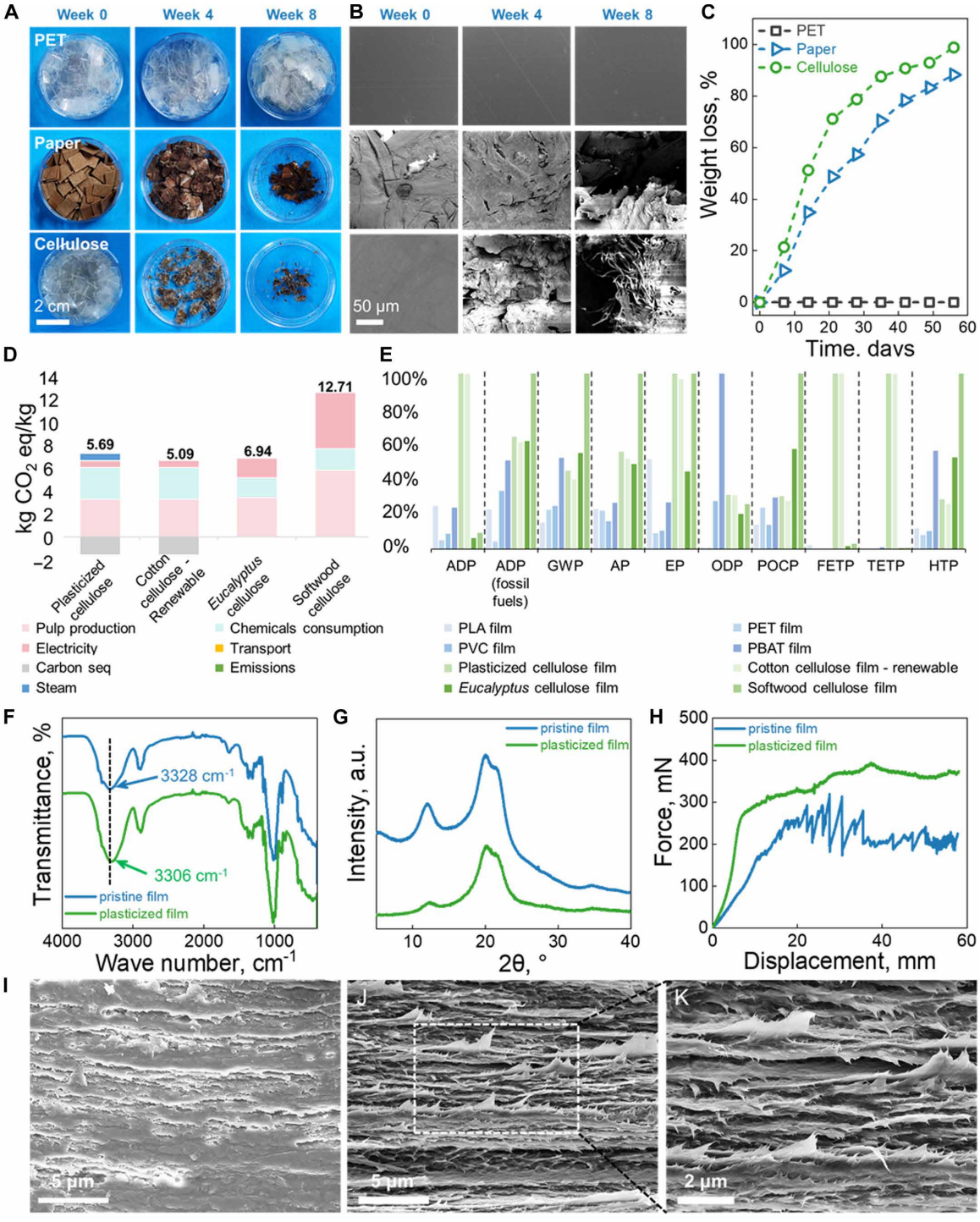

Fig. 2. Biodegradation, sustainability, and plasticization. (**A**) Photographs of PET, paper, and plasticized cellulose films during the biodegradation process. (**B**) Scanning electron microscopy (SEM) images of PET, paper, and plasticized cellulose films at different biodegradation time and (**C**) the corresponding weight loss curves. (**D**) GWP contribution analysis of cotton cellulose film and cotton cellulose film—renewable, *Eucalyptus* cellulose film and softwood cellulose film. (**E**) Comparison of LCA results of PLA film, PET film, PVC film, PBAT film, cotton cellulose film, and cotton cellulose film—renewable, *Eucalyptus* cellulose film and softwood cellulose film. (**F**) Attenuated total reflectance Fourier transformed infrared spectra. (**G**) Wide-angle x-ray diffraction profile. (**H**) Force-displacement curve from the tearing test of both pristine and plasticized cellulose films. (**I**) SEM images of pristine cellulose films. SEM images of plasticized cellulose films on (**J**) low and (**K**) high magnification.

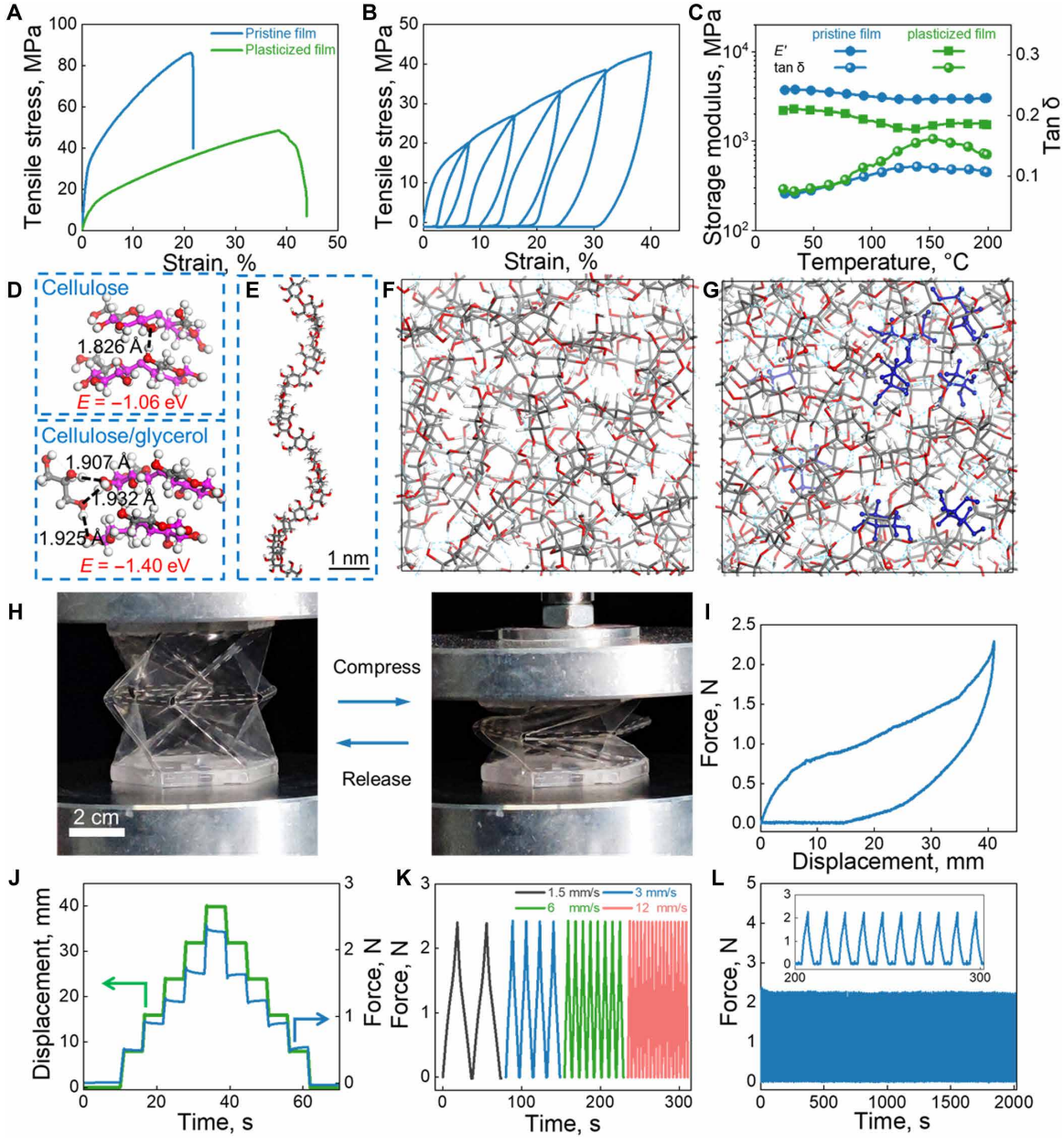

Fig. 3. Mechanical performance of cellulose films and the plasticized cellulose film-assembled sustainable origami. (**A**) Tensile stress-strain curves of pristine and plasticized cellulose films. (**B**) Tensile loading-unloading cycles with successive increasing strain of the plasticized cellulose films. (**C**) Dynamic mechanical analysis test of the pristine and plasticized cellulose films as a function of temperature. (**D**) Theoretical calculation of energy-optimized geometry of binding between cellulose-cellulose and cellulose-glycerol. (**E**) Molecular model of a cellulose chain. (**F**) Molecular structure snapshots of pristine cellulose and (**G**) plasticized cellulose. (**H**) Photographs of sustainable origami before and after compression. (**I**) Compressive loading-unloading force-displacement curve of sustainable origami. (**J**) Compressive response of sustainable origami under a series of step-up displacement of 8 mm to a maximum of 40 mm followed by step-down displacement to the initial state. (**K**) Compressive loading-unloading cycles with successive increasing displacement of the sustainable origami. (**L**) Compressive loading-unloading curves of sustainable origami for 200 cycles at 40 mm displacement.

remain relatively stable over time at ambient conditions, with a slight increase in tensile strength and Young's modulus, while a marginal decrease in tensile strain (fig. S6). The storage modulus of both pristine and plasticized cellulose films stabilizes at a high level throughout the entire temperature range (Fig. 3C), demonstrating their outstanding thermal mechanical stability, further confirming the reliability of the films.

To gain further insights of cellulose-glycerol interactions and plasticization, the binding energy of noncovalent interactions was calculated via molecular dynamics (MD) in anhydrous environment. The binding energy notably decreases to −1.42 eV after the introduction of glycerol within cellulose in the structure optimization calculations (Fig. 2D), suggesting that strong hydrogen bonds form between cellulose and glycerol. The interactions within a box with cellulose chains [degree of polymerization (DP) = 10] and glycerol molecules are further calculated and statistically count to verify the hydrogen bonds variation after plasticization (Fig. 2, E to G). The number of hydrogen

bonds within the simulation box increased from 338 to 413 (fig. S7A). The 413 hydrogen bonds in cellulose-glycerol system are categorized into three parts: 333 of cellulose-cellulose interaction, 66 of cellulose-glycerol interaction, and 14 of glycerol-glycerol interactions. The formation of cellulose-glycerol hydrogen bonds slightly reduces the cellulose-cellulose hydrogen bond interaction, thus plasticized the cellulose chains (*46*). Moreover, the length of the cellulose-cellulose hydrogen bonds increases, while the angle decreases after plasticization (fig. S7, B to F), indicating the downward of cellulose-cellulose hydrogen bonds intensities (*47*), which is responsible for hampering the formation of cellulose II crystalline structure after plasticization, and decreases the Young's modulus of the resultant films (Figs. 2G and 3A) (*48*). Similar to glycerol, other polyalcohol can also hinder the formation and reduce the intensity of cellulose-cellulose hydrogen bonds while introduce many cellulose-polyalcohol hydrogen bonds (figs. S8 and S9), which may also lead to substantial plasticization effect of cellulose films.

To demonstrate the capability of high-strength cellulose films in origami-based soft robotic systems, a two-level Kresling origami is constructed using laser-cut cellulose films as panels and a pair of 3D printed transparent resin sheets as top and bottom boards (the geometrical design of the cellulose films panel and resin boards are shown in fig. S10). Kresling origami has been adopted as an ideal building block for soft robots due to its large contraction/deployment capabilities and omnidirectional bending (*49*). The mechanical properties of the assembled Kresling origami are tested in compression mode to evaluate the reliability of the origami structure for soft robotic applications. Pristine cellulose films tend to break at the creases under folding after laser-cutting and are thus not suitable for origami construction (fig. S11). In contrast, plasticized cellulose film panels remain structural integrity under repetitive compressing-releasing cycles (Fig. 3D). Finite element analysis (FEA) simulation of the origami shew that the strain concentrated in and near the creases (with a maximum strain of 7.25%), while the panels exhibited low strain during the whole compressing process (fig. S12). The force required to compress the origami increases under compressing, reaching a maximum of 2.4 ± 0.2 N at displacement of 40 mm, and then returns to the initial value upon release (Fig. 3E), facilitating easy operation. Furthermore, during a stepwise compression test with an 8-mm step size at a speed of 10 mm/s followed by a 5-s hold, the force remains stable during each hold (Fig. 3F), showing no creep effect as the displacement reaches a maximum of 40 mm and then returns to the initial state over multiple steps. When the origami structure undergoes compression to a maximum 40-mm displacement at various speeds (adjusting the bending speed is common in practical applications for human-robot interactions), the force response remains stable (Fig. 3G). Moreover, the origami structure consistently displays repetitive force response to a maximum 40-mm displacement more than 200 loading-unloading cycles, with a maximum force variation throughout the test decreasing by only 1.2% (Fig. 3H). Moreover, the appearance and mechanical property of the sustainable Kresling origami remains almost unchanged (fig. S13), demonstrating exceptional stability and reliability of the sustainable cellulose-based origami structure.

Self-sensing origami structure

To equip the deformable origami structure with self-sensing capabilities, sustainable salt-infused gelatin organogels are produced by simply mixing and heating gelatin with other additives in deionized water. This mixture solidifies within 10 min under ambient conditions after being poured and cast into a petri dish (Fig. 1B and see Materials and Methods for details) (*19*). As demonstrated in fig. S14, the gelatin organogels can be stretched to more than 600% strain, achieving ultimate tensile stresses and Young's modulus of 0.72 ± 0.13 MPa and 0.31 ± 0.02 MPa, respectively (fig. S14A). The highly coiled gelatin molecules are responsible for the high extensibility, while the addition of small molecules such as sugar and glycerol, acting as cosolvents, enhances the mechanical properties of the gelatin gels by substantially facilitating helix-helix association between gelatin chains (*50*). In practical scenarios, sensors are expected to withstand multiple loading-unloading cycles. Consequently, the cyclic tensile performance is assessed (fig. S14, B to D), showing a series of hysteresis loops between successive loading-unloading cycles. These loops result from the loading-induced breaking and partial recovery of the physical bonds during the unloading process, which dissipates the mechanical energy applied to the organogels. Furthermore, the gelatin organogels can undergo loading-unloading cycles under 100% strain more than 200 times, demonstrating outstanding mechanical stability. In addition, the gelatin-based organogels adhere well to various substrates, including our plasticized cellulose films, copper sheets, and glass slides (fig. S14, E to G), indicating their broad applicability as sustainable sensors. Specifically, the peeling force/width of cellulose films from gelatin organogels reach 16.9 $N{\cdot}m^{-1}$ (fig. S15), which confirming the excellent adhesiveness between cellulose films and gelatin organogels layers.

For practical applications, the dehydration of the organogels is a critical factor affecting sensor performance. To assess this, weight loss curves and relative resistance changes are measured during storage under ambient conditions for durations up to 340 days. The gelatin organogels exhibits only 1% loss of their weight after 24 hours, 8% after 15 days of storage, and 9% after storing for 340 days (fig. S16A). In addition, the resistance of the organogels remains stable throughout the long-term dehydration process (fig. S16B), the long-term storage stability further underscoring the suitability of the gelatin organogels as sensing materials.

Next, sustainable gel-based sensors are fabricated by solidifying gelatin solution atop plasticized cellulose films (see Materials and Methods for details and fig. S17). The resistive variation of these gelatin organogels under bending deformation is then tested. These sensors successfully endure repetitive bending-releasing deformations without interfacial failure (fig. S18A), confirming the strong adhesion between the organogel sensors and the plasticized cellulose films. The resistance of the sensor increases proportionally by 7% as the compressive displacement reaching 40 mm (fig. S18B), a result of the elongated ion transmission pathway during bending (*51*). Subsequently, the resistance change of the gelatin organogels under a step-and-hold test is measured, involving alternating stepwise bending. The applied displacement increases to 40 mm using 8-mm step size at a speed of 10 mm/s, holding for 5 s at each step before decreasing back to zero in the same manner (fig. S18C). Similar to the mechanical response shown in Fig. 3I, the resistance change induced by bending remains stable during each hold, with no obvious creep effect observed. In addition, the relative resistance change at different bending speeds is also recorded. Even when bent to a displacement of 40 mm, the maximum difference in relative resistance does not decrease as the bending speed increases from 1.5 to 12 mm/s, indicating the velocity-insensitive performance of the gelatin organogel sensors. Furthermore, the displacement

sensing capability remains stable over 200 loading-unloading cycles with negligible attenuation when bending to a 40-mm displacement, indicating the excellent sensing stability and durability of the gelatin organogels.

The Kresling origami design preserves a hollow interior space throughout its high-ratio folding and deploying process (*35*, *36*), allowing for a seamless integration of three slender sensing sheets coated with gelatin organogels inside the origami shell. This integration forms a complete sustainable self-sensing origami module when connected with two 3D printed end plates (Fig. 4A and fig. S19). The obtained sustainable self-sensing origami can undergo reversible compressing-releasing cycles (Fig. 4A), thanks to the structural elasticity of both the origami shell and the inner sensing sheets (Fig. 3D and fig. S18A). When uniaxially compressed with a displacement of 40 mm, all three sensing sheets uniformly undergo bending deformations and exhibit similar relative resistance changes of about 7.8% (Fig. 4B and fig. S20), demonstrating consistent and reliable sensor performance. Localized pressing, which induces bending deformations in different sections of the origami structure, results in different resistance changes across three sensing sheets. This differential response facilitates the discrimination of bending directions, a feature that will be explored further in subsequent sections. In addition, the step-and-hold test results exhibit a series of stable plateaus during each holding step, with no noticeable resistance change throughout the test (Fig. 4C). The relative resistance changes of the organogel-based sensing sheets under different compressing speeds also show a velocity-insensitive performance, similar to the behavior of the pristine organogels under bending (Fig. 4D and fig. S18D). This confirms the applicability of the sustainable self-sensing origami in closed-loop robotic systems. Furthermore, the self-sensing origami module exhibits excellent stability in its sensing performance under cyclic compression-release deformations with displacements up to 40 mm, maintaining a consistent performance over more than 200 cycles (Fig. 4E). In addition, the resistance changes behavior of the gelatin sensors under loading/unloading cycles for 200 times remains stable after resting for 20 min and even after storing for 1 week after the initial 200 loading/unloading cycles (fig. S21), indicating the superior long-term stability of the sensors. The stable and linear sensor signals render the sustainable self-sensing origami highly suitable and readily adaptable for use in subsequent soft robotic systems.

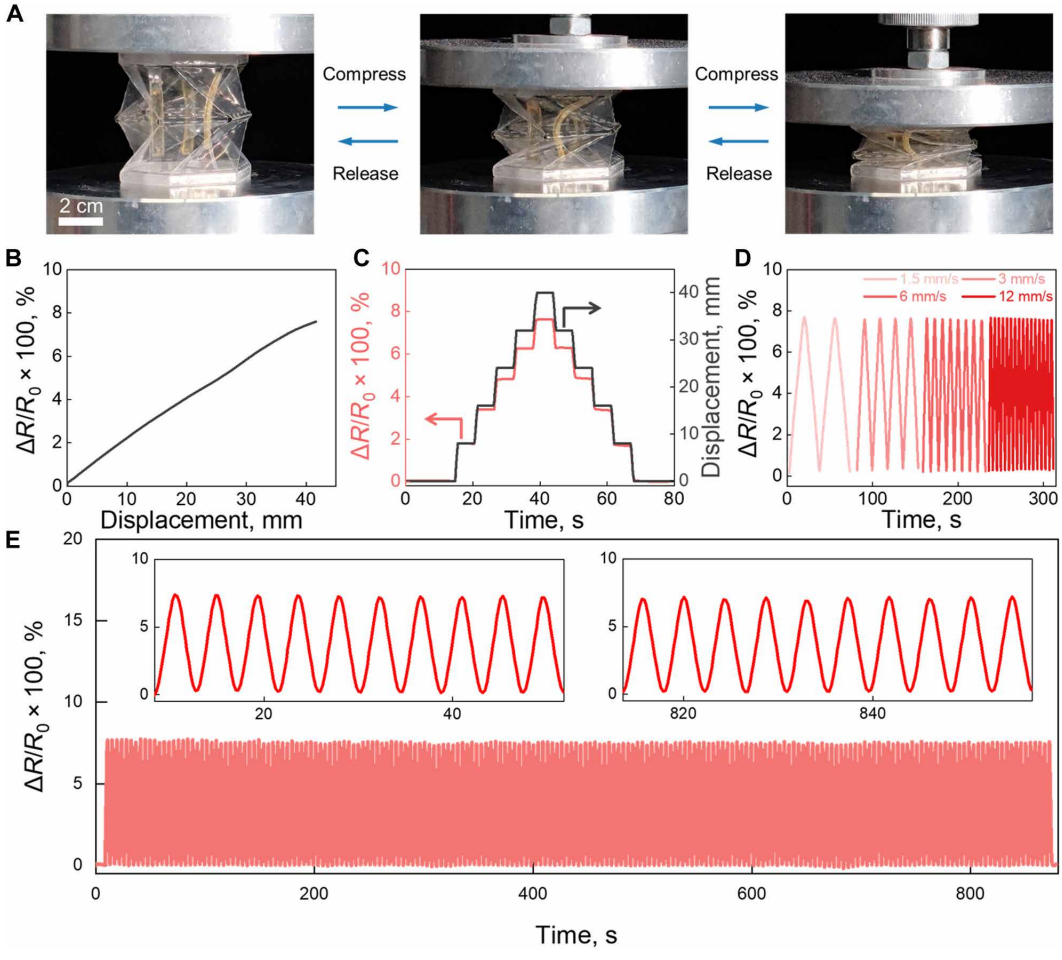

Fig. 4. Characterization of the sensory performance on the sustainable self-sensing origami. (**A**) Photographs of the compressing-release cycle of the sustainable self-sensing origami. (**B**) Relative resistance change of the sustainable self-sensing origami during uniaxial compressing. (**C**) Relative resistance change of the self-sensing origami under a series of step-up compressive displacement of 5 mm to a maximum of 40 mm followed by step-down displacement to the initial state. (**D**) Relative resistance change of the self-sensing origami on the compressive loading-unloading cycles with a displacement of 40 mm at different loading speed. (**E**) Relative resistance change of the self-sensing origami more than 200 loading/unloading cycles at 40-mm displacement, with close-up views at the beginning and end of the test.

Closed-loop soft robotic system

The present sustainable, elastic self-sensing module, integrated on a Kresling origami pattern, is capable of generating multi-modal deformations including contraction, extension, and omnidirectional bending. This versatility makes it suitable for constructing both control interfaces (i.e., rocker) and manipulative devices (i.e., robotic arm). Consequently, an eco/human-friendly, closed-loop soft robotic system that can enables interaction with operators and completion of teleoperation tasks has been developed using the identical origami modules (Fig. 5A). The rocker used for human-robot interaction is constructed using a single self-sensing origami module featuring a two-level Kresling pattern. This module can be compressed by the operator, transmitting sensing signals to the manipulator for remote control via wireless transmission systems. Harnessing the modular structure of the self-sensing origami, the robotic arm can be readily constructed by connecting several modules in series. Here, four identical modules are adopted to form a continuum robotic arm with an initial length of 240 mm. To control the three–degree of freedom motion of the robotic arm, three cotton cables, each connected to a motor and the distal end of the robotic arm, pass through holes on the plates of each module to create motion constraints throughout the arm. The stability of the origami modules leads to a mechanically robust robotic arms, which can maintain its original shape after bending and then, rotating for more than 100 cycles (fig. S22 and movie S1). Controlled by sensing signals from the rocker, the motors drive the robotic arm via the three cables, achieving contraction/extension through synchronous activation of the three motors and bending via their differential actuation (fig. S23). Simultaneously, deformations of the robotic arm are captured by the self-sensing modules, relayed to a PC, and translated into a virtual robotic avatar that mirrors the arm's movements in real time, and monitored remotely by the operator. Thus, a seamless human-in-the-loop teleoperation system is constructed (Fig. 5A).

As demonstrated in Fig. 4B, the resistance change ($\Delta R/R_0$) in the self-sensing origami increases with the compressive displacement. Within a single Kresling origami module, the $\Delta R/R_0$ values for the three organogels sensors (marked as A, B, and C) vary when the origami is bent in different directions, reflecting the distinct deformations each sensor undergoes. This mechanism allows for the generation of seven distinct signals when pressure is individually applied to the center and each of the six corners of the origami (Fig. 5, B and C). Compressing the center of the rocker results in similar $\Delta R/R_0$ curves for all three sensors (Fig. 5D, channel 1). However, when corners 1 to 7 are compressed, the peak $\Delta R/R_0$ values for each sensor diverge notably (Fig. 5D, channels 2 to 7). For example, case 3 (i.e., pressing corner 3) features relatively large and almost symmetric resistance change for sensors A and C and relatively smaller resistance change for sensor B; case 5 (i.e., pressing corner 5) shows a decreasing trend in resistance change from sensors A to C. These variations stem from the geometrical nature of the Kresling origami and the placements of these three sensors. This differential response enables precise determination of bending direction by comparing the relative $\Delta R/R_0$ magnitudes among the three sensors, as their resistance change ratios distinctly vary with pressure applied to different parts of the rocker. These seven signals serve as inputs to remotely control the four-module origami robotic arm, enabling it to perform various motions (Fig. 5, E to H). In addition, with the 12-channel resistance variation data collected from the self-sensing robotic arm, the operator can guide the avatar on the screen to reflect the current motion status (fig. S24), allowing for remote control of the robotic arm to execute various motion tasks via the rocker and monitor its status without the need for additional visual systems (Fig. 5, I to L, and movie S2). This integrated sensing and control system enhances the operability and responsiveness of the robotic arm, ensuring effective human-robot interaction.

DISCUSSION

This paper introduces a dual closed-loop, origami-based robotic system that is both eco-friendly and robotically versatile. Using mechanically robust cellulose films for the origami structures and gelatin organogels for sensing—both of which are fully biodegradable and sustainable—we have developed self-sensing origami robots. These robots are designed in a modular fashion, capable of multimodal deformations such as contraction, extension, and omnidirectional bending. This functionality enhances human-robot interaction, serving dual roles as robotic arms and as interfaces for remote control operations. This integrated sensing and control system enhances the operability and responsiveness of the robotic arm, ensuring effective and intuitive human-robot interaction. In teleoperation scenarios such as hazardous material handling and environmental exploration, this system will enable operators to perform various tasks with precision and confidence while maintaining simple and durable functional units that are environment friendly. Future expansions of this work could explore three main avenues: (i) the development of high-strength, tough, and electrically conductive sustainable materials for directly integrated, self-sensing soft robots to increase the robustness of the robotic systems and adapt more complex robotic tasks; (ii) the development of effective scaling-up methodologies for mass production of sustainable materials to further reduce the environmental impact of the materials and explicit more suitable application scenarios of sustainable robots; and (iii) the implementation of alternative actuation methods (e.g., pneumatic or electrical) into more complex robotic systems to achieve fast and precise movement in sustainable soft robots and substantially improve the robotic performance. The design and construction methods proposed in this study aim to enhance the utilization of sustainable materials and technologies, expanding their potential for integrating various soft robotic systems in an environmentally friendly manner and paving the way toward a more sustainable future for our community.

MATERIALS AND METHODS

Chemicals and materials

Cotton linter pulp with a viscosity-average molecular weight (M_η) 8.3×10^4 g/mol was provided by Hubei Chemical Fiber Co. Ltd. (Xiangyang, China) and was used as our source of cellulose. Sodium hydroxide (NaOH), sodium chloride (NaCl), sodium alginate, CMCNa, urea, glycerol, gelatin, citric acid, and sucrose were purchased from Sinopharm Chemical Regent Co. Ltd. (Shanghai, China). All raw materials and chemicals were used as received, without any further treatment.

Fabrication of sustainable cellulose films

Cellulose was dissolved in a precooled aqueous NaOH/urea solution according to the previous report (*52*). Initially, 6 g of cotton linter

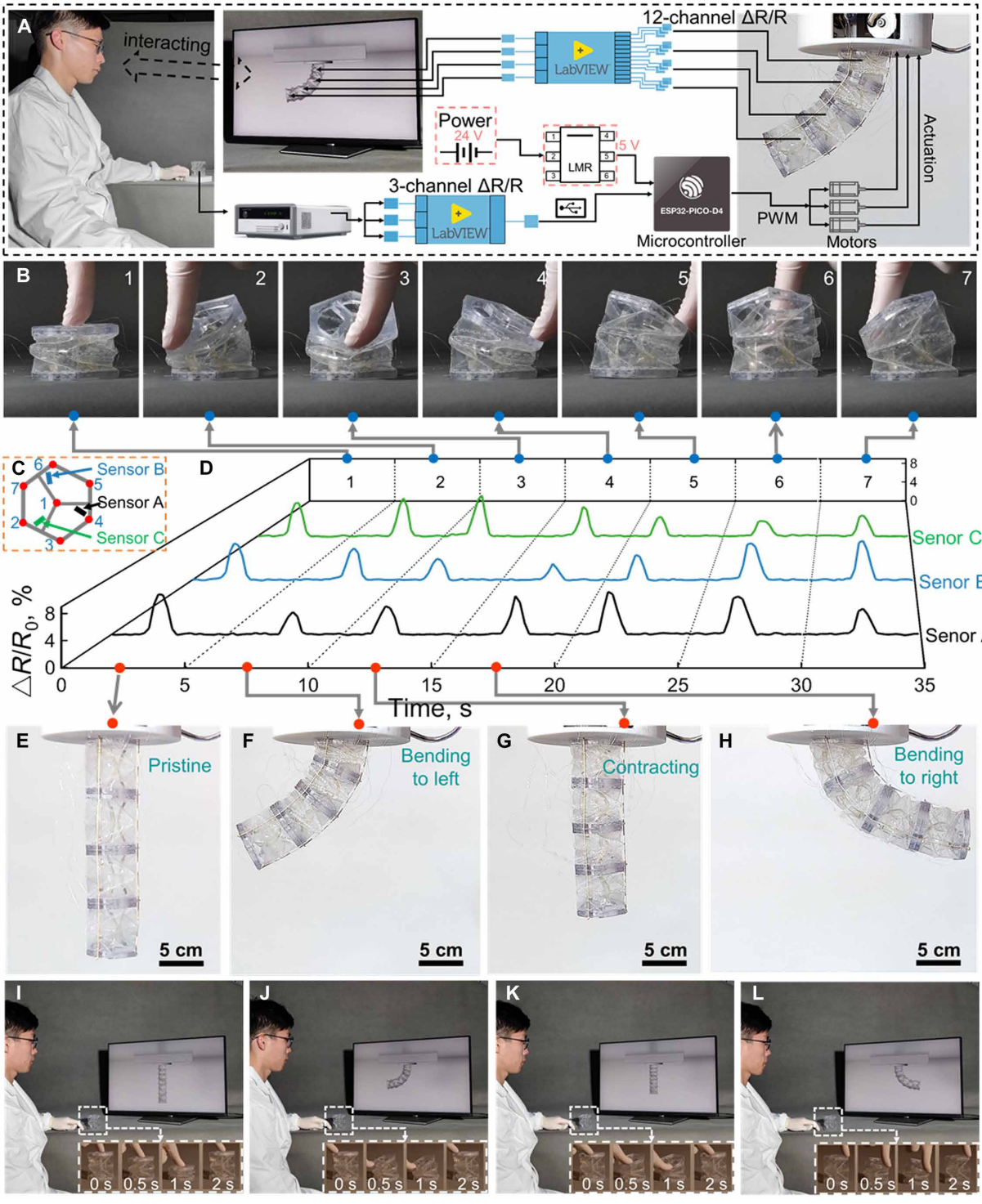

Fig. 5. Closed-loop human-robot interaction using a sustainable origami rocker to teleoperate a sustainable robotic arm. (**A**) Overall workflow of closed-loop human-robot interactions. (**B**) Photographs of the operator compressing on different positions of the sustainable origami rocker for seven input modes. (**C**) Illustration of different positions on the moving platform of the origami. (**D**) Corresponding relative resistance change of the three gelatin organogels sensors inside the origami structure. (**E** to **H**) Front-view photographs of the moving process of the sustainable robotic arm from (E) the pristine position to (F) left bending, (G) contracting, and (H) right bending. (**I** to **L**) Photographs of the teleoperation process on the operator's side, corresponding to (E) to (H), respectively.

pulp was added to a 7/12 weight % (wt %) NaOH/urea solution precooled to −12°C. After vigorous stirring, a clear, viscous 6 wt% cellulose solution was obtained. This solution was then evenly spread and cast on a glass plate to form a 2-mm-thick layer, with bubbles removed using a centrifuge. The cast cellulose solution was subsequently immersed and coagulated in deionized water to induce the formation of a physically crosslinked structure. After being thoroughly rinsed with deionized water, cellulose hydrogels were obtained. These hydrogels were then further immersed in a deionized water bath at room temperature with 3 wt % glycerol for 24 hours. Last, 0.2-mm–thick plasticized cellulose films were obtained after being dried at 60°C for 4 hours. In addition, the 0.1-mm–thick and 0.05-mm–thick plasticized cellulose films were obtained with the same procedure when 1-mm–thick and 0.5-mm–thick cellulose hydrogels were casted, respectively. For comparison, pristine cellulose films were produced by directly drying the hydrogels at 60°C without undergoing the glycerol water bath treatment.

Fabrication of sustainable gelatin-based ionic conductive gels and sensors

The sustainable gelatin-based ionic gels were prepared using a modified version of a previously reported procedure (*19*). Initially, 2.5 g of sucrose, 0.5 g of citric acid, 0.5 g of NaCl, and 4 g of glycerol were dissolved in 2 g of deionized water. Subsequently, 3.3 g of gelatin powder was added to this solution and allowed to swell for 24 hours at ambient temperature. The mixture was then heated in an oven at 60°C with moderate stirring until the gelatin was completely dissolved. After centrifuging to remove air bubbles, the gelatin solution was poured into a petri dish and left to cool at room temperature under ambient conditions, resulting in the formation of ionic conductive gelatin gels.

The process of integrating the sustainable sensors is depicted in fig. S17. First, plasticized cellulose films were cut into rectangular sheets measuring 60 mm in length, 5 mm in width, and 0.1 mm in thickness. The previously prepared gelatin-based solution was then cast onto these molds on the surface of cellulose sheets and left to cool and solidify at room temperature under ambient conditions. The resulting gelatin-based organogel dimensions were 35 mm in length, 5 mm in width, and 1 mm in thickness. To finalize the sensor, a 0.05-mm–thick cellulose film was applied over the surface of the gel to prevent dehydration, thus completing the fabrication of ionically conductive gelatin organogel-based sensors. The as-prepared gelatin organogel sensors were stored in a humidity chamber at temperature of 25°C and humidity of 50%.

Fabrication of self-sensing Kresling origami and robotic arm

The structure of Kresling origami has been extensively studied (*53*). Plasticized cellulose films (0.2-mm thickness) were cut into a predefined geometry of two-level Kresling patterns to avoid any rotation during deformation (fig. S10A) using a laser cutting instrument (CMA0601-G-A, Han's Yueming Laser Group Co., Ltd., China). Each single origami unit was assembled by securing the laser-cut cellulose films between two rigid flat 3D printed resin boards (J826 Prime 3D printer, Stratasys Ltd., USA) (fig. S10B) using a biodegradable gelatin glue. Three independent gelatin-based organogels were then integrated within the Kresling origami structure between the corresponding upper and bottom boards. This integration results in the formation of self-sensing Kresling origami unit. A self-sensing Kresling origami robotic arm was subsequently produced by connecting four of these self-sensing units in series.

Material characterization

Mechanical properties—including tensile and compressive strain-stress curves, peel force-displacement curve—were measured using a universal material testing machine (Instron 5943, USA) at a tensile speed of 5 mm/min according to ISO 527-1:2019 (E). The rectangular cellulose films with dimensions of 75 mm in length, 10 mm in width, and 0.2 mm in thickness were used for tensile tests. Three parallel samples were used for each test. The Young's modulus for each sample was calculated from the initial linear region of the stress-strain curves. Tearing tests of rectangular cellulose films (150 mm in length, 50 mm in width, and 0.2 mm in thickness, with a 75-mm-long slit in the middle of the sample along the length direction) were conducted at a speed of 200 mm/min according to ISO 6383-1:2015 to obtain the fracture toughness (Γ). For tearing test, three parallel specimens were tested. Specifically, Γ was calculated according to the formula $\Gamma = 2F/t$, where F is the stable-state tearing force and t is the thickness of membrane. FTIR spectra were acquired using a Nicolet 5700 FTIR Spectrometer (Thermo Fisher Scientific, USA). Dynamic mechanical analysis (DMA) was performed using a DMA Q800 (TA Instruments, USA). WAXD profiles were acquired using a D8 Advance diffractometer equipped with a Cu Kα radiation source (λ = 0.154 nm) (Bruker, USA). Scanning electron microscope (SEM) images were obtained from Zeiss Gemini 500 microscope (Thermo Fisher Scientific, USA) with 5-kV operating voltage.

Life cycle assessment

LCA methodology was applied to evaluate the life cycle environmental impacts of 1 kg of cellulose film based on ISO 14040 and ISO 14044 (*54*). The "cradle-to-gate" system for the cellulose film production includes the cultivation and transportation of cotton, the pulping of cotton, production of chemicals and energy used, and direct emissions in the film production (fig. S3). The carbon sequestered in the film is accounted based on its carbon content. The film is compared with other cellulose films and fossil-based film whose inventory data are shown in tables S1 and S2. The environmental impact analysis was performed using Simapro (V9.5). The LCIA method CML 2001 was applied and environmental impact include abiotic depletion (ADP, kg Sb eq), abiotic depletion fossil fuels (ADP fossil fuels, MJ), GWP (GWP 100a, kg CO_2/kg), acidification (AP, kg SO_2 eq), eutrophication (EP, kg PO_4^{3-} eq), ODP (kg CFC-11 eq), photochemical oxidation (POCP, kg C_2H_4 eq), fresh water aquatic ecotoxicity (FETP, kg 1,4-DB eq), terrestrial ecotoxicity (TETP, kg 1,4-DB eq), and human toxicity (HTP, kg 1,4-DB eq).

MD simulation

Molecular models of cellulose (with a degree of polymerization of 10) and glycerol were constructed using Materials Studio software package (*55*). The electronic structure was described using the polymer consistent force field 3.1 force field. The electrostatic and van der Waals interactions were evaluated using the Ewald method and atom-based approaches, respectively. Temperature and pressure were controlled via the Anderson and Berendsen algorithms. The energy convergence was achieved with a tolerance of 10^{-5} kcal/mol, while the force convergence criterion was set to 10^{-4} kcal/mol/Å. Annealing simulations were used to fully relax the system. After equilibrating the systems under a 300 K and 1 atm of NPT ensemble for 100 ps, hydrogen bonds were identified using the following criteria: a hydrogen-donor distance of less than 3.21 Å, and a donor-hydrogen-acceptor angle greater than 90° (*56*). The binding energies of cellulose and

cellulose, cellulose, and glycerol in an anhydrous environment were also performed via MD calculation.

FEA simulation

To investigate the compression behavior of the sustainable Kresling origami structure, a numerical simulation was performed using ABAQUS-Explicit (Dassault Systems Inc., France). The thin-walled structure was modeled using shell elements with a thickness of 0.2 mm, while the top and bottom support plates were treated as rigid bodies. During the simulation, a downward compression displacement of 40 mm was applied to the support plates. The density of the material was set at 1450 kg/m^3, measured from plasticized cellulose films. The material properties of the cellulose films in the Kresling origami structure were defined with a nonlinear elastic model, with Young's modulus of 1 GPa and Poisson's ratio of 0.45, representing a moderately stiff and elastic material. This explicit dynamic method accurately captured the structural response during rapid deformation and ensured solution stability, even under large deformation conditions.

Soil degradation test

The PET, paper, and plasticized cellulose films sheets were separately enclosed within 300-mesh nylon fabrics and then buried approximately 20 cm beneath the soil in the campus of Westlake University (fig. S2A). The environment temperature range during the soil degradation test was recorded (fig. S2B). The degraded samples were taken out every 7 days after buried to the soil, rinsed thoroughly with deionized water, followed by drying under vacuum at 60°C for 24 hours. The weight loss percentage of the samples at different degradation time was calculated according to the formula: weight loss $= ((m_1 - m_0)/m_0) \times 100\%$, where m_0 and m_1 are the weight of samples before and after soil degradation. The morphological images of 0-, 4-, and 8-week-degraded cellulose films were recorded using SEM (Zeiss Gemini 500, Thermo Fisher Scientific, USA).

Sensor characterization

An automated sensor testbed was built using a motorized uniaxial stage for characterizing the electrical performance of the sensor under pure bending deformation (fig. S25). The data were collected from the sensors using a Keysight 34972A data acquisition unit (Keysight Technologies Inc., USA), with controlled speeds for different test cycles. The stage was set to move at a controlled speed of 6 mm/s for all tests, except when assessing the change in resistance as a function of different loading speeds. Repeatability and durability of the sensors were also evaluated by loading-unloading testing with 200 cycles for each sensing element. The electrical resistance curves of the gelatin sensors were real time and automatically averaged in the software for every 100 data points collected.

Supplementary Materials

The PDF file includes:
Figs. S1 to S25
Tables S1 to S4
Legends for movies S1 and S2

Other Supplementary Material for this manuscript includes the following:
Movies S1 and S2

REFERENCES AND NOTES

1. R. Pearson, The threat and promise of robots. *Nature* **325**, 560–560 (1987).
2. C. A. Aubin, B. Gorissen, E. Milana, P. R. Buskohl, N. Lazarus, G. A. Slipher, C. Keplinger, J. Bongard, F. Iida, J. A. Lewis, R. F. Shepherd, Towards enduring autonomous robots via embodied energy. *Nature* **602**, 393–402 (2022).
3. J. Cui, J. Trinkle, Toward next-generation learned robot manipulation. *Sci. Robot.* **6**, eabd9461 (2021).
4. D. Rus, M. T. Tolley, Design, fabrication and control of soft robots. *Nature* **521**, 467–475 (2015).
5. M. Hägele, K. Nilsson, J. N. Pires, R. Bischoff, "Industrial robotics" in *Springer Handbook of Robotics*, B. Siciliano, O. Khatib, Eds. (Springer International Publishing, 2016), pp. 1385–1422.
6. T. Kim, S. Lee, T. Hong, G. Shin, T. Kim, Y.-L. Park, Heterogeneous sensing in a multifunctional soft sensor for human-robot interfaces. *Sci. Robot.* **5**, eabc6878 (2020).
7. Z. Zhang, Y. Long, G. Chen, Q. Wu, H. Wang, H. Jiang, Soft and lightweight fabric enables powerful and high-range pneumatic actuation. *Sci. Adv.* **9**, eadg1203 (2023).
8. Y. Yu, J. Li, S. A. Solomon, J. Min, J. Tu, W. Guo, C. Xu, Y. Song, W. Gao, All-printed soft human-machine interface for robotic physicochemical sensing. *Sci. Robot.* **7**, eabn0495 (2022).
9. P. Rothemund, Y. Kim, R. H. Heisser, X. Zhao, R. F. Shepherd, C. Keplinger, Shaping the future of robotics through materials innovation. *Nat. Mater.* **20**, 1582–1587 (2021).
10. D. Hu, F. Giorgio-Serchi, S. Zhang, Y. Yang, Stretchable e-skin and transformer enable high-resolution morphological reconstruction for soft robots. *Nat. Mach. Intell.* **5**, 261–272 (2023).
11. S. Song, F. Fallegger, A. Trouillet, K. Kim, S. P. Lacour, Deployment of an electrocorticography system with a soft robotic actuator. *Sci. Robot.* **8**, eadd1002 (2023).
12. S. Y. Kim, Y. Choo, R. A. Bilodeau, M. C. Yuen, G. Kaufman, D. S. Shah, C. O. Osuji, R. Kramer-Bottiglio, Sustainable manufacturing of sensors onto soft systems using self-coagulating conductive pickering emulsions. *Sci. Robot.* **5**, eaay3604 (2020).
13. W. Liu, Y. Duo, J. Liu, F. Yuan, L. Li, L. Li, G. Wang, B. Chen, S. Wang, H. Yang, Y. Liu, Y. Mo, Y. Wang, B. Fang, F. Sun, X. Ding, C. Zhang, L. Wen, Touchless interactive teaching of soft robots through flexible bimodal sensory interfaces. *Nat. Commun.* **13**, 5030 (2022).
14. Y. Zhao, Q. Li, Z. Liu, Y. Alsaid, P. Shi, M. Khalid Jawed, X. He, Sunlight-powered self-excited oscillators for sustainable autonomous soft robotics. *Sci. Robot.* **8**, eadf4753 (2023).
15. J. Shi, Y. Dai, Y. Cheng, S. Xie, G. Li, Y. Liu, J. Wang, R. Zhang, N. Bai, M. Cai, Y. Zhang, Y. Zhan, Z. Zhang, C. Yu, C. F. Guo, Embedment of sensing elements for robust, highly sensitive, and cross-talk–free iontronic skins for robotics applications. *Sci. Adv.* **9**, eadf8831 (2023).
16. M.-H. Oh, Y.-H. Kim, S.-M. Lee, G.-S. Hwang, K.-S. Kim, Y.-N. Kim, J.-Y. Bae, J.-Y. Kim, J.-Y. Lee, Y.-C. Kim, S. Y. Kim, S.-K. Kang, Lifetime-configurable soft robots via photodegradable silicone elastomer composites. *Sci. Adv.* **9**, eadh9962 (2023).
17. H. Na, Y.-W. Kang, S. Park Chang, S. Jung, H.-Y. Kim, J.-Y. Sun, Hydrogel-based strong and fast actuators by electroosmotic turgor pressure. *Science* **376**, 301–307 (2022).
18. F. Hartmann, M. Baumgartner, M. Kaltenbrunner, Becoming sustainable, the new frontier in soft robotics. *Adv. Mater.* **33**, e2004413 (2020).
19. M. Baumgartner, F. Hartmann, M. Drack, D. Preninger, D. Wirthl, R. Gerstmayr, L. Lehner, G. Mao, R. Pruckner, S. Demchyshyn, L. Reiter, M. Strobel, T. Stockinger, D. Schiller, S. Kimeswenger, F. Greibich, G. Buchberger, E. Bradt, S. Hild, S. Bauer, M. Kaltenbrunner, Resilient yet entirely degradable gelatin-based biogels for soft robots and electronics. *Nat. Mater.* **19**, 1102–1109 (2020).
20. A. Heiden, D. Preninger, L. Lehner, M. Baumgartner, M. Drack, E. Woritzka, D. Schiller, R. Gerstmayr, F. Hartmann, M. Kaltenbrunner, 3D printing of resilient biogels for omnidirectional and exteroceptive soft actuators. *Sci. Robot.* **7**, eabk2119 (2022).
21. T. Benselfelt, P. Rothemund, P. S. Lee, Ultrafast, high-strain, and strong uniaxial hydrogel actuators from recyclable nanofibril networks. *Adv. Mater.* **35**, 2300487 (2023).
22. E. H. Rumley, D. Preninger, A. Shagan Shomron, P. Rothemund, F. Hartmann, M. Baumgartner, N. Kellaris, A. Stojanovic, Z. Yoder, B. Karrer, C. Keplinger, M. Kaltenbrunner, Biodegradable electrohydraulic actuators for sustainable soft robots. *Sci. Adv.* **9**, eadf5551 (2023).
23. X. Huang, L. Liu, Y. H. Lin, R. Feng, Y. Shen, Y. Chang, H. Zhao, High-stretchability and low-hysteresis strain sensors using origami-inspired 3D mesostructures. *Sci. Adv.* **9**, eadh9799 (2023).
24. D. Rus, M. T. Tolley, Design, fabrication and control of origami robots. *Nat. Rev. Mater.* **3**, 101–112 (2018).
25. T. Li, C. Chen, A. H. Brozena, J. Y. Zhu, L. Xu, C. Driemeier, J. Dai, O. J. Rojas, A. Isogai, L. Wågberg, L. Hu, Developing fibrillated cellulose as a sustainable technological material. *Nature* **590**, 47–56 (2021).
26. Y. Ye, L. Yu, E. Lizundia, Y. Zhu, C. Chen, F. Jiang, Cellulose-based ionic conductor: An emerging material toward sustainable devices. *Chem. Rev.* **123**, 9204–9264 (2023).
27. Z. Li, C. Chen, H. Xie, Y. Yao, X. Zhang, A. Brozena, J. Li, Y. Ding, X. Zhao, M. Hong, H. Qiao, L. M. Smith, X. Pan, R. Briber, S. Q. Shi, L. Hu, Sustainable high-strength macrofibres extracted from natural bamboo. *Nat. Sustain.* **5**, 235–244 (2022).
28. H. Zhu, W. Luo, P. N. Ciesielski, Z. Fang, J. Y. Zhu, G. Henriksson, M. E. Himmel, L. Hu, Wood-derived materials for green electronics, biological devices, and energy applications. *Chem. Rev.* **116**, 9305–9374 (2016).
29. J. Cai, S. Kimura, M. Wada, S. Kuga, L. Zhang, Cellulose aerogels from aqueous alkali hydroxide-urea solution. *ChemSusChem* **1**, 149–154 (2008).

30. D. Ye, X. Lei, T. Li, Q. Cheng, C. Chang, L. Hu, L. Zhang, Ultrahigh tough, super clear, and highly anisotropic nanofiber-structured regenerated cellulose films. *ACS Nano* **13**, 4843–4853 (2019).
31. B. E. Droguet, H.-L. Liang, B. Frka-Petesic, R. M. Parker, M. F. L. De Volder, J. J. Baumberg, S. Vignolini, Large-scale fabrication of structurally coloured cellulose nanocrystal films and effect pigments. *Nat. Mater.* **21**, 352–358 (2021).
32. R. Saberi Riseh, Advancing agriculture through bioresource technology: The role of cellulose-based biodegradable mulches. *Int. J. Biol. Macromol.* **255**, 128006 (2024).
33. L. Chen, T. Qiang, X. Chen, W. Ren, H. J. Zhang, Fabrication and evaluation of biodegradable multi-cross-linked mulch film based on waste gelatin. *Chem. Eng. J.* **419**, 129639 (2021).
34. S. J. Jong, K. KarunaKaran, M. E. Wasli, Z. Musa, S. F. Chin, Cellulose-based hydrogel as a natural medium for paddy seed germination. *Starch Stärke* **76**, 2200234 (2024).
35. C. Zhang, Z. Zhang, Y. Peng, Y. Zhang, S. An, Y. Wang, Z. Zhai, Y. Xu, H. Jiang, Plug & play origami modules with all-purpose deformation modes. *Nat. Commun.* **14**, 4329 (2023).
36. Q. Ze, S. Wu, J. Dai, S. Leanza, G. Ikeda, P. C. Yang, G. Iaccarino, R. R. Zhao, Spinning-enabled wireless amphibious origami millirobot. *Nat. Commun.* **13**, 3118 (2022).
37. H. Nadeem, P. Nimmegeers, W. Batchelor, P. Billen, Cellulose nanofibre films as a substitute for plastic packaging: A comparative environmental life cycle assessment. *Food Bioprod. Process.* **145**, 175–186 (2024).
38. P. Zhu, A. Vo, X. Sun, Y. Zhang, M. Mandegari, S. Zargar, Q. Tu, J. Zhu, Z. Yu, H. Sun, D. Zheng, F. Jiang, Water-induced controllable deswelling strategy enabled rapid fabrication of transparent cellulose film for plastics replacement. *Chem. Eng. J.* **492**, 152200 (2024).
39. S.-J. Zhou, D. Zhang, S.-J. Xiong, Q. Liu, X. Shen, S. Yu, Z. Sun, J. Wen, L. Wang, T.-Q. Yuan, A high-performance and cost-effective PBAT/montmorillonite/lignin ternary composite film for sustainable production. *ACS Sustainable Chem. Eng.* **12**, 14704–14715 (2024).
40. S. Van Nguyen, B.-K. Lee, Microfibrillated cellulose film with enhanced mechanical and water-resistant properties by glycerol and hot-pressing treatment. *Cellul.* **28**, 5693–5705 (2021).
41. N. Isobe, S. Kimura, M. Wada, S. Kuga, Mechanism of cellulose gelation from aqueous alkali-urea solution. *Carbohydr. Polym.* **89**, 1298–1300 (2012).
42. I. Mena-Prado, E. Navas-Ortiz, M. Fernández-García, E. Blázquez-Blázquez, S. Limbo, M. Rollini, D. M. Martins, A. M. Bonilla, A. del Campo, Enhancing functional properties of compostable materials with biobased plasticizers for potential food packaging applications. *Int. J. Biol. Macromol.* **280**, 135538 (2024).
43. Y. Liu, S. Liu, Z. Liu, Y. Lei, S. Jiang, K. Zhang, W. Yan, J. Qin, M. He, S. Qin, J. Yu, Enhanced mechanical and biodegradable properties of PBAT/lignin composites via silane grafting and reactive extrusion. *Compos. Part B Eng.* **220**, 108980 (2021).
44. P. Wei, J. Huang, Y. Lu, Y. Zhong, Y. Men, L. Zhang, J. Cai, Unique stress whitening and high-toughness double-cross-linked cellulose films. *ACS Sustainable Chem. Eng.* **7**, 1707–1717 (2019).
45. H. Zhu, S. Zhu, Z. Jia, S. Parvinian, Y. Li, O. Vaaland, L. Hu, T. Li, Anomalous scaling law of strength and toughness of cellulose nanopaper. *Proc. Natl. Acad. Sci. U.S.A.* **112**, 8971–8976 (2015).
46. H. Yan, J. Wang, C. Du, Z. Li, H. Yuan, Z. Xu, Y. Tan, Hydrogen bond-mediated strong plasticization for high-performance alginate plastics. *Adv. Mater.* **36**, e2400648 (2024).
47. Y. Li, C. Chang, Z. Zhu, L. Sun, C. Fan, Terahertz wave enhances permeability of the voltage-gated calcium channel. *J. Am. Chem. Soc.* **143**, 4311–4318 (2021).
48. M. Chen, T. Runge, L. Wang, R. Li, J. Feng, X.-L. Shu, Q.-S. Shi, Hydrogen bonding impact on chitosan plasticization. *Carbohydr. Polym.* **200**, 115–121 (2018).
49. S. Wu, Q. Ze, J. Dai, N. Udipi, G. H. Paulino, R. Zhao, Stretchable origami robotic arm with omnidirectional bending and twisting. *Proc. Natl. Acad. Sci. U.S.A.* **118**, e2110023118 (2021).
50. S. Shimizu, N. Matubayasi, Gelation: The role of sugars and polyols on gelatin and agarose. *J. Phys. Chem. B* **118**, 13210–13216 (2014).
51. Y. Ye, Y. Zhang, Y. Chen, X. Han, F. Jiang, Cellulose nanofibrils enhanced, strong, stretchable, freezing-tolerant ionic conductive organohydrogel for multi-functional sensors. *Adv. Funct. Mater.* **30**, 2003430 (2020).
52. J. Cai, L. Zhang, Rapid dissolution of cellulose in LiOH/urea and NaOH/urea aqueous solutions. *Macromol. Biosci.* **5**, 539–548 (2005).
53. L. Lu, S. Leanza, R. R. Zhao, Origami with rotational symmetry: a review on their mechanics and design. *Appl. Mech. Rev.* **75**, 050801 (2023).
54. I. O. f. Standardization, environmental management: Life cycle assessment; requirements and guidelines. ISO Geneva (2006).
55. K. Mazeau, L. Heux, Molecular dynamics simulations of bulk native crystalline and amorphous structures of cellulose. *J. Phys. Chem. B* **107**, 2394–2403 (2003).
56. R. Kumar, J. R. Schmidt, J. L. Skinner, Hydrogen bonding definitions and dynamics in liquid water. *J. Chem. Phy.* **126**, 204107 (2007).

Acknowledgments: We acknowledge the Research Center for Industries of the Future (RCIF) at Westlake University and Westlake Education Foundation for supporting this work. The authors thank Instrumentation and Service Center for Physical Sciences, Instrumentation and Service Center for Molecular Sciences, and Westlake Center for Micro/Nano Fabrication at Westlake University for the facility support and technical assistance. **Funding:** This work was supported by the National Key R&D Program of China (2024YFB4707500) and the National Natural Science Foundations of China (grants 12350003 and 52205031). **Author contributions:** Conceptualization: P.W., Z.Z., and H.J. Methodology: P.W., Z.Z., S.C., L.E., J.L., L.W., and H.J. Investigation: P.W., Z.Z., S.C., Y.M., M.T., L.E., W.Y., Y.Z., Y.W., J.Z., C.X., J.L., L.W., and H.J. Visualization: P.W., Z.Z., S.C., and W.Y. Supervision: J.L, L.W., and H.J. Writing—original draft: P.W., Z.Z., S.C., and H.J. Writing—review and editing: P.W., Z.Z., Y.M., M.T., J.L., L.W., and H.J. **Competing interests:** The authors declare that they have no competing interests. **Data and materials availability:** All data needed to evaluate the conclusions in the paper are present in the paper and/or the Supplementary Materials.

Submitted 25 July 2024
Accepted 9 January 2025
Published 7 February 2025
10.1126/sciadv.ads0217